EXTRACTION OF DAMAGED REGIONS USING SAR DATA AND NEURAL NETWORKS

Yosuke ITO[†], Masafumi HOSOKAWA[††], Hoonyol LEE[‡], Jian Guo LIU[‡]
[†]Department of Civil Engineering, Takamatsu National College of Technology, Japan
ito@takamatsu-nct.ac.jp
[††]Earthquake Disaster Section, National Research Institute of Fire and Disaster, Japan
hosokawa@fri.go.jp
[‡]T. H. Huxley School of Environment, Earth Science and Engineering,
Imperial College of Science, Technology and Medicine, U.K.
hoonyol.lee@ic.ac.uk, j.g.liu@ic.ac.uk

Working Group III/4

KEY WORDS: Classification, Coherence, Decorrelation, Earthquakes, Interferometry, LVQ, Multi-temporal.

ABSTRACT

This paper presents classification results using neural networks based on INSAR coherence imagery data for evaluation of the damage of Kobe earthquake in 1995. Coherence derived from multi-temporal SAR data before and after an earthquake presents a temporal decorrelation in disturbed regions. As L-band SAR data is more robust than C-band SAR data for spatial and temporal decorrelation, we used multi-source and temporal SAR coherence images derived from interferometric pairs of JERS-1 and ERS-1 single look complex images (SLCs). Hazard areas can be estimated by classifying two categories defined as the damaged regions and otherwise using set of the coherence images. A neural classifier was used because of requiring no assumption for probability distribution function of each category. A competitive neural network trained by the learning vector quantization (LVQ) was adopted to the neural classifier in consideration of generalization ability and convergence. Total five coherence images were produced using effective interferometric pairs derived from two JERS-1 and four ERS-1 SLCs. The average coherence of JERS-1 is higher and has significantly higher contrast than that of ERS-1 even though the spatial decorrelation and the temporal separation are nearly equal. A hazard survey map was used for assessing extraction results. The LVQ method generated 23% higher kappa coefficient by adding the JERS-1 coherence and produced better results than the maximum likelihood method from the view point of balance of the number of the correctly classified pixels.

1 INTRODUCTION

It is an important research topic to identify regions damaged by an earthquake. Synthetic aperture radar (SAR) data, in particular, is a valuable information source to define and classify damaged regions as it is not affected by cloud cover and contains the phase information highly sensitive to surface change. A strong earthquake can cause tremendous destruction in an urban area such as structure collapse and liquefaction. Furthermore, a conflagration can burn many buildings in urban circumstances. Land surface of a damaged region can be dramatically changed by the earthquake.

Coherence derived from multi-temporal SAR data before and after the earthquake presents temporal decorrelation. An antenna pattern depending on SAR instrument and water vapor in the atmosphere does not affect the coherence. Coherence can thus be utilized to detect changes caused by the earthquake and to identify the damaged regions (Yonezawa and Takeuchi, 1999). Coherence as a local correlation can be affected by temporal, spatial and thermal decorrelation factors (Zebker and Villasenor, 1992). The theoretical spatial decorrelation is a function of SAR system parameters and a target location such as wavelength, radar bandwidth, slant range, perpendicular baseline and local terrain slope (Lee and Liu, 1999). L-band SAR data is more robust than C-band SAR data for the spatial decorrelation because the wavelength of L-band ($23.53cm$) is much longer than that of C-band ($5.66cm$). An L-band coherence image is more useful in a case of an interferometric pair with long temporal separation (Fujisawa and Rosen, 1998). Unfortunately, JERS-1 was terminated on 11^{th} October 1998. There are only limited interferometric image pairs available as the result of poorer orbit control than ERS.

Hazard areas can be estimated by discriminating two categories defined as damaged regions and otherwise, using coherence images. In general, it is difficult to assume a probability distribution function (PDF) of the coherence values in each category since these categories are determined based on land survey results and include various objects on the surface. It is thus effective to employ a non-parametric classifier that does not require any assumption for the PDF (Ito and Omatu, 1997).

Table 1: Summary of JERS-1 and ERS-1 data acquisition

Satellite	Acquisition date	Precipitation (mm)	SLC name
JERS-1 (L-band)	9 Sep. 1992	0.0	J1
	6 Feb. 1995	0.0	J2
ERS-1 (C-band)	1 Nov. 1992	1.5	E1
	12 Sep. 1993	0.0	E2
	27 Feb. 1996	0.0	E3
	7 May 1996	0.0	E4

Table 2: Interferometric pairs of SAR data

Satellite	SLC name Master	SLC name Slave	Temporal separation ($days$)	Perpendicular baseline (m)	Spatial decorrelation	Coherence name
JERS-1	J1	J2	881	225	0.96	JC1-2
ERS-1	E1	E2	315	140	0.84	EC1-2
		E3	1283	107	0.88	EC1-3
		E4	1353	44	0.95	EC1-4
	E2	E3	898	33	0.96	EC2-3
		E4	968	96	0.89	EC2-4

In this paper, we propose an approach of neural network (NN) classification for extracting the damaged regions using multi-source and temporal SAR coherence images. Among several known NN structures, we employed the learning vector quantization (LVQ) as the NN for its merits of generalization ability, learning efficiency and good convergence (Kohonen, 1997).

2 SAR DATA DESCRIPTION

The study area is densely inhabited districts in Kobe, Japan. The Hyogoken Nanbu earthquake, 7.2 magnitude, hit this area on 17^{th} January 1995. About 200,000 structures collapsed in the study area and 5.2% of the collapsed area was burned. In a reclaimed land, subsidence caused by liquefaction resulted in destabilised structures and deformed roads.

Table 1 is a summary of JERS-1 and ERS-1 SAR data acquisition. Single look complex images (SLC) were produced by compressing SAR raw data. To generate the precision SLCs of JERS-1, we applied low pass filtering to eliminate microwave interference from ground radar systems and compensated the sensitivity time control and the automatic gain control. The path number of both SAR scenes is 72. The row numbers are 242 for JERS-1 and 243 for ERS-1. All scenes were acquired in a descending mode. Total six scenes of the multi-temporal JERS-1 and ERS-1 were used in the experiment of methodology. Figure 1 shows the study area in a three look amplitude image of J1 where mountain and sea areas are masked off. There is a densely built-up area in the central part of figure 1. Several dark lines indicate major roads. Port-Island is one of the reclaimed lands. We choose the SAR data such that the earthquake event is included within temporal separation of an interferometric pair which has an adequate baseline to produce a coherence image. The scenes acquired before the earthquake are J1, E1 and E2 and after the earthquake are J2, E3 and E4. Daily precipitation on the dates of data acquisition shown in table 1 were observed by the Kobe marine meteorological observatory.

Table 2 shows temporal separation (D), perpendicular baseline ($B_\perp$) and theoretical spatial decorrelation (ρ_s) for all the interferometric pairs. Here, the spatial decorrelation ρ_s is calculated as

$$\rho_s = 1 - \frac{c}{\lambda \cdot r \cdot B_w} B_\perp |\cot(\theta_0 - \alpha)| \tag{1}$$

where θ_0 is the nominal incidence angle of the radar on the ellipsoidal earth, α the local terrain slope, λ the radar wavelength, r the slant range, B_w the frequency bandwidth of the transmitted chirp signal, and c the velocity of light (Lee and Liu, 1999). As the study area is almost flat, we assume $\alpha = 0^\circ$. JC1-2 is the coherence image derived from J1 and J2. Similarly, EC1-2, EC1-3, etc., denote the coherence images derived from the relevant ERS-1 SLC pairs. The ρ_s of JC1-2 is higher than that of EC1-4 despite JC1-2 has longer $B_\perp$. The coherence images that contain information of the damage caused by th earthquake are JC1-2, EC1-3, EC1-4, EC2-3 and EC2-4. EC1-2 is the coherence image derived from before event pair.

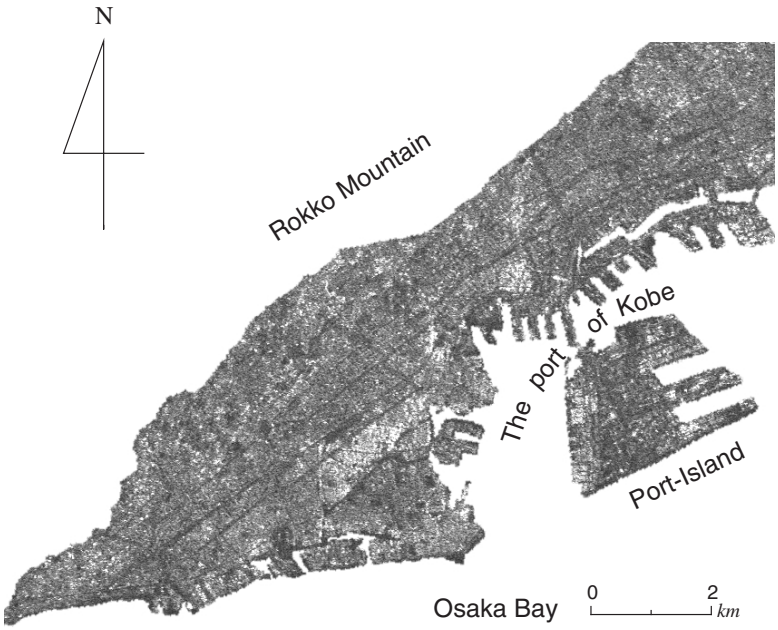

Figure 1: Three look amplitude image of J1 in Kobe, Japan

3 COHERENCE IN DAMAGED REGIONS

Coherence at each pixel is estimated by

$$\gamma = \frac{|\langle E_1 E_2^* \rangle|}{\sqrt{\langle |E_1|^2 \rangle} \sqrt{\langle |E_2|^2 \rangle}} \tag{2}$$

where E_1 and E_2 are SLC values, * and $\langle \cdot \rangle$ denote complex conjugation and ensemble averaging, respectively. After applying the earth flattening to an initial interferogram, γ was computed between master and slave SLCs based on 16 pixels taken in the azimuth direction and 4 pixels in the range direction in consideration of the standard deviation (SD) required for the classification. All coherence pixels were resampled to approximately $30m$ squared area after being converted from slant range to ground range geometrically. The coherence can be modelled as

$$\gamma = \rho_n \cdot \rho_t \cdot \rho_s \tag{3}$$

where ρ_n is the thermal noise of the SAR system and ρ_t the temporal decorrelation (Zebker and Villasenor, 1992). We can assume $\rho_n = 1$ since the signal-to-noise ratios for both SAR systems are high enough for this study. If the coherence image is derived from a SLC pair across the earthquake event, ρ_t is affected by the changes caused by the earthquake and other temporal effects and therefore becomes lower in the damaged regions than in the undamaged regions.

The SLCs of two interferometric pairs: J1 and J2; E2 and E3, were acquired under almost the same weather and time conditions except $B_\perp$ and SAR system parameters. Figures 2 (a) and (b) show the coherence images of JC1-2 and EC2-3 for comparison of radar wavelength effects. Histograms of JC1-2 and EC2-3 are presented in figure 3. The coherence of JC1-2 is considerably higher and has significantly higher contrast than that of EC2-3 as shown in figures 2 and 3 even though they have nearly equal ρ_s and D. Robustness for L-band SAR coherency is thus convincingly demonstrated.

On the other hand, as EC1-2 (figure5 (a)) is derived from two SLCs before the earthquake, it has no relation to the earthquake and includes land use information only. As shown in figure 5 (b), the histogram of EC1-2 indicates higher coherence than those of JC1-2 and EC2-3. The extraction approach using the decorrelation by surface change can essentially apply to regions with the high coherence only. This will eliminate the areas subject to temporal decorrelation not relevant to the earthquake. Hence, the study area is reduced such that $\gamma \geq 0.6$ in EC1-2.

Figure 4 shows a hazard map surveyed by Ministry of Construction and Architectural Institute of Japan in 1995. The map was rasterised to $30m \times 30m$ to correspond to the coherence images in pixel by pixel. Black dots in the map indicate burned or completely collapsed structures. These black dots are expressed as the damaged category (ω_1) and the others are defined as category (ω_2) in the map. The coherence of the damaged regions tends to fall down in figures 2 (a) and (b). The surface changes caused by the earthquake evidently bring about this phenomenon. To assess the distribution for ω_1 and ω_2 in all the coherence images, mean values and SDs of the coherence value for each category are calculated as illustrated in figure 6. Here, $|$ denotes the mean value and the both side ranges are $\pm$SD. All coherence images have

(a) JC1-2 (L-band, $D = 881days$ and $B_\perp = 225m$) (b) EC2-3 (C-band, $D = 898days$ and $B_\perp = 33m$)

Figure 2: Coherence images with decorrelation cause by earthquake

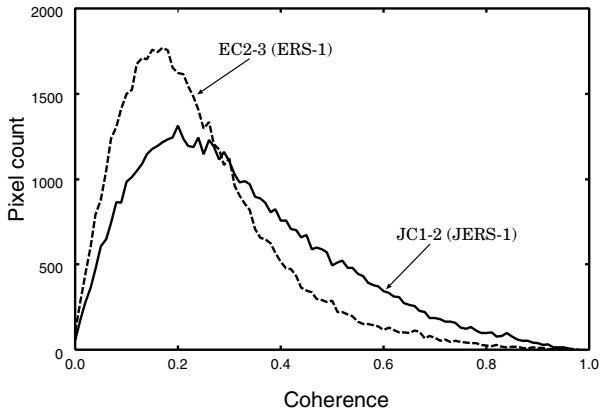

Figure 3: Histograms of JC1-2 and EC2-3

Figure 4: Hazard survey map

a similar distribution, that is, the mean value of ω_1 is lower than that of ω_2. Divergence between ω_1 and ω_2 for JC1-2 is more evident than those for the ERS-1 coherence images even though the distributions are considerably overlapped. This tendency is also shown in figure 2. It is interesting to notice for EC1-2 that the distribution of ω_1 and ω_2 are largely overlapped and ω_1 has slightly higher average than ω_2. This hints that the damaged areas are mostly build-up areas which are temporally stable without the earthquake. As a result of the coherence distribution shown in figure 6, a possibility of detecting the damaged regions using the multi-source coherence is suggested.

4 EXTRACTION METHOD

The neural classifier for the extraction method is outlined in figure 7. It generally has a higher ability for classification of remote sensing data, although its structure and learning algorithm are simpler than the back-propagation method for well-known NNs. Coherence value $[0.0, 1.0]$ is applied to each neuron as an input vector $\mathbf{x} = [x_1, \ldots, x_N]^t$ where N denotes the number of neurons at the input layer. The number of output neurons M is a constant value multiplied by the number of categories ($L = 2$). Input signals are exposed to the input layer and each signal is transmitted to all of the neurons in the competitive layer through their connection weights. After competing with each other in the Euclidean distance between the input vector and neuron weight, a winner is found and output as one and the other outputs are equal to zero. Each neuron in the competitive layer is assigned to one of the predetermined categories $\omega_k, k = 1, \ldots, L$. The category must be assigned to a relevant number of neurons since it includes various objects with individual decorrelation. A category ω_k is thus represented by using a set of neuron weights. The competitive NN is trained by the LVQ method. The LVQ cyclically update the weight vectors so as to reward correct classification and punish incorrect ones.

Kohonen (1997) proposed that LVQ1, LVQ2.1 and OLVQ1 algorithms for the LVQ method. After preliminary experiments, we employ the following training approach;

(1) Move the weight vectors roughly by the LVQ1.
(2) Tune up the weight vectors in category boundaries by the LVQ2.1, where window parameter $w = 0.3$.

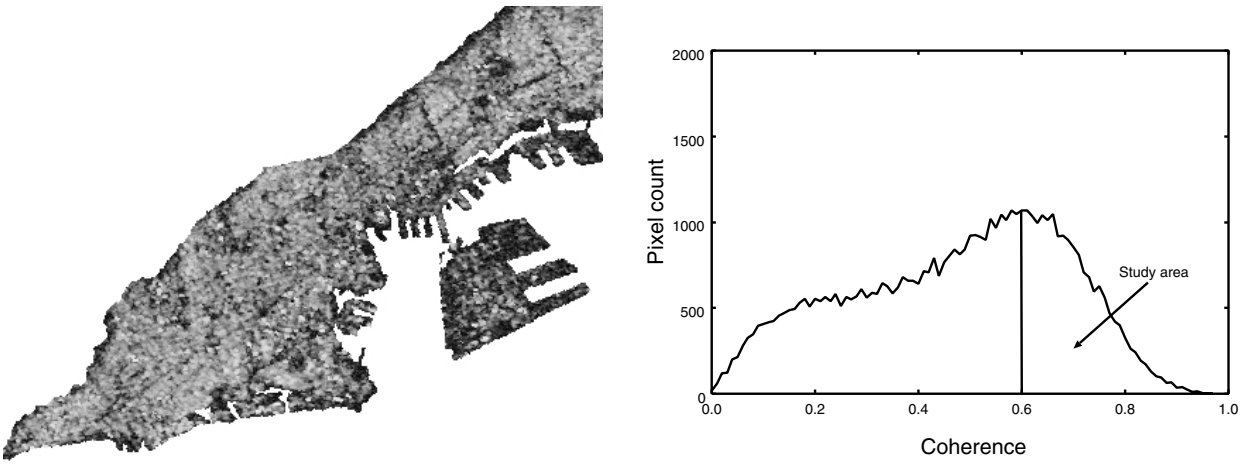

(a) Coherence image (b) Histogram

Figure 5: EC1-2 derived from before event pair

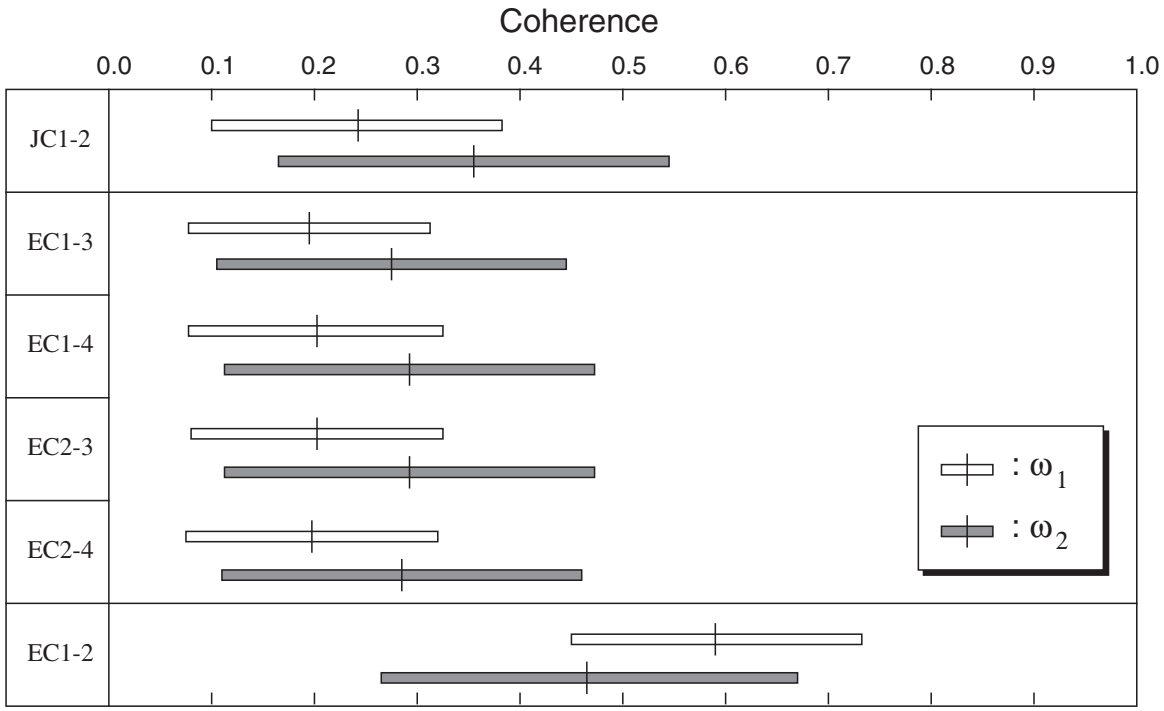

Figure 6: Coherence distribution for categories ω_1 and ω_2

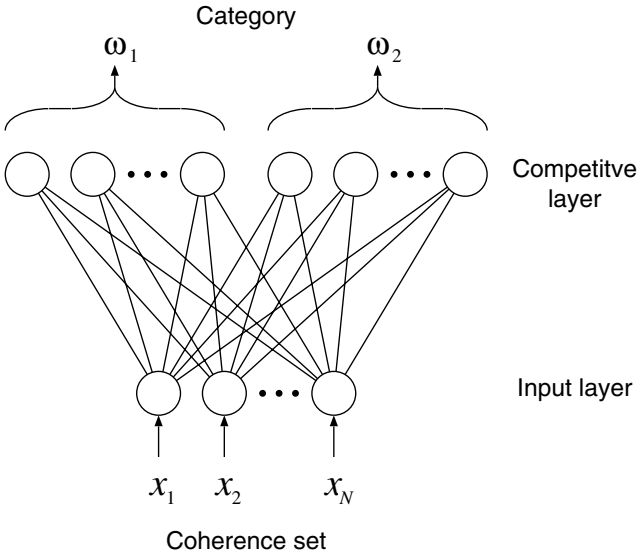

Figure 7: Structure of competitive neural network

The LVQ2.1 behaves effectively when the PDFs are overlapped each other. In both procedures, the initial learning rate is set to 0.03 and the weight vectors are repeatedly updated 40000 times. The extraction method exposes the coherence images with unknown category to the trained NN and classifies it as the category to which the winner neuron belongs.

To find out the effectiveness of the multi-source coherence images for extracting the damaged regions, we defined two types of coherence sets: $C_1 = \{$EC1-3, EC1-4, EC2-3, EC2-4$\}$; $C_2 = C_1 + \{$JC1-2$\}$. The number of coherence images corresponds to the number of input neurons N.

In the experiments, the training and test data (table 3) were chosen from the area covered by either the burned or the completely collapsed structures based on the hazard surveying map in figure 4. The training data of ω_1 and ω_2 are 5×5 and 10×10 resampled scenes from the test data, respectively. The LVQ method was compared with the maximum likelihood (ML) method. All classification methods employed the same training and test data for a fair comparison.

5 RESULTS AND DISCUSSION

Extraction results of damaged regions were assessed with regard to an kappa coefficient (Richards, 1993) and distribution of the extracted regions in the classified image. Confusion matrix $A = [a_{ij}], i, j = 1, \ldots, L$ is produced for each classification result where a_{ij} denotes the number of pixels classified ω_i into ω_j. The kappa coefficient (κ) is defined by

$$\kappa = \frac{a_{++} \sum_{k=1}^{L} a_{kk} - \sum_{k=1}^{L} a_{k+} a_{+k}}{a_{++}^2 - \sum_{k=1}^{L} a_{k+} a_{+k}} \tag{4}$$

where $a_{++} = \sum_{i=1}^{L} \sum_{j=1}^{L} a_{ij}$, $a_{i+} = \sum_{j=1}^{L} a_{ij}$ and $a_{+j} = \sum_{i=1}^{L} a_{ij}$.

Figure 8 shows the comparisons between C_1 and C_2 for the LVQ and ML methods in term of κ where the number of neurons M in the competitive layer varies from 2 to 20 to find out an optimum NN. For C_1 and C_2 when Ms are equal to 4 and 6, the NNs produce the maximum accuracy. The changes of κ with the number of neurons M are small for C_1 since the distributions of ω_1 and ω_2 in the coherence images of C_1 are similar as shown in figure 6. However, κ for C_2 is sensitive to the number of neurons M since the distributions of JC1-2 and the other ERS coherence images are different. The κ of the LVQ using the optimum NN is higher than that of the ML for both coherence sets.

To assess the classification accuracy for all combinations about the classifiers and the coherence sets, the kappa coefficient (κ) is shown in table 4. The κ is improved 23% (0.035) in the LVQ and 34% (0.039) in the ML methods by adding JC1-2. It is also improved 31% (0.035) in C_1 and 20% (0.031) in C_2 by applying the LVQ method. Table 5 shows the confusion matrices using C_2. The LVQ method produces better results than the ML method from the view point of balance of the number of the correctly classified pixels, that is, a_{11} of the LVQ decreases 418 and a_{22} increases 2198 compared with the

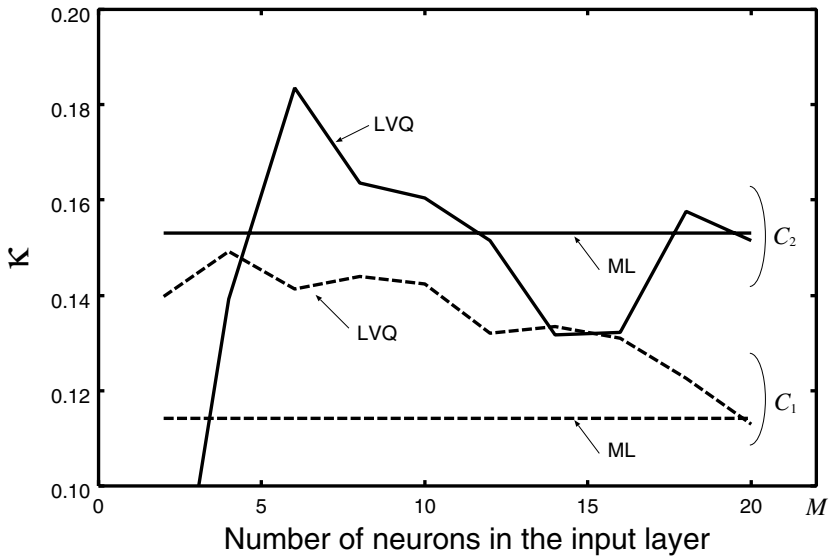

Figure 8: Comparison with kappa coefficient (κ) using LVQ and ML methods

Table 3: Training and test data

Category	Training data	Test data
ω_1	131	2994
ω_2	150	16221
Total	281	19215

(pixels)

Table 4: Assessment of kappa coefficient

Coherence set	Classifier	κ
C_1	LVQ ($M = 4$)	0.149
	ML	0.114
C_2	LVQ ($M = 6$)	0.184
	ML	0.153

ML. As a result of using the ML, the test data tend to be classified into ω_1. These results mean that the non-parametric approach is more significant when the PDFs are unknown.

Finally, we show the classification images using C_2 in figures 9 (a) and (b) which are generated by the LVQ with $M = 6$ and the ML methods, respectively. As the extracted pixels using the ML are too many (table 5 (b)), the extraction regions of the LVQ result in figure 9 (a) is more similar to the hazard map (figure 4) than those of the ML result in figure 9 (b). It is experimentally shown that the classification results can be improved using the multi-source coherence image and the neural classifier.

6 CONCLUSIONS

We have produced and assessed classified images for extraction of damaged regions by using multi-source and temporal coherence images and classification methods. It is suggested that extraction accuracies can be improved by using the multi-source coherence images and the neural classifier on an experimental basis. In comparison with the parametric method, the LVQ produces higher classification accuracy in term of the kappa coefficient. For future study, we will consider an extraction method which can classify the coherence images into more detailed categories according to degree of collapse. To enhance the detection accuracy, it is desirable that the damaged regions are roughly specified based on coseismic crustal deformation using differential interferogram.

Table 5: Confusion matrices using C_2

(a) LVQ with $M = 6$

$[a_{ij}]$		Result ω_1	ω_2	Total
Test data	ω_1	1978	1016	2994
	ω_2	5799	10422	16221
	Total	7777	11438	19215

(pixels)

(b) ML

$[a_{ij}]$		Result ω_1	ω_2	Total
Test data	ω_1	2396	598	2994
	ω_2	7997	8224	16221
	Total	10393	8822	19215

(pixels)

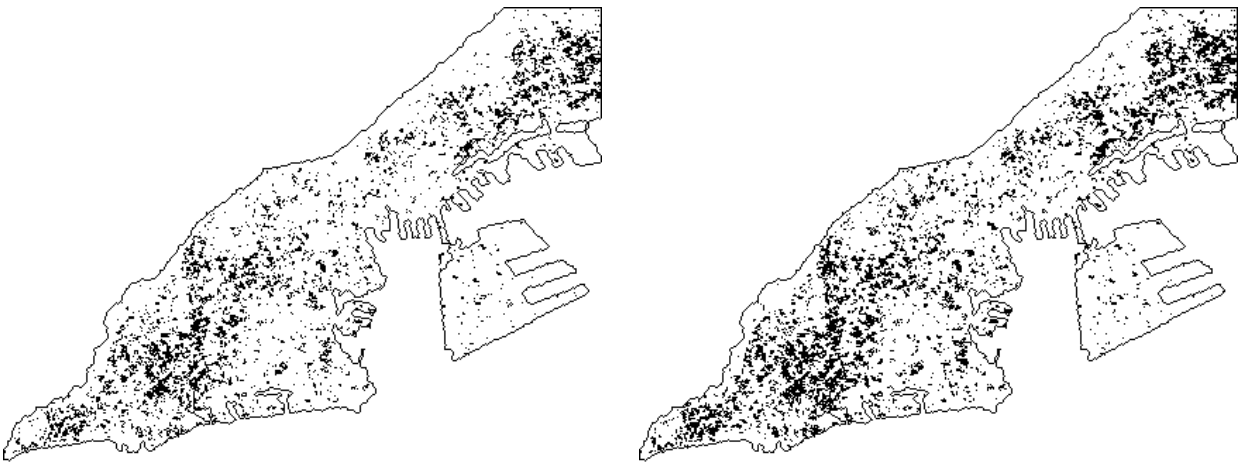

(a) LVQ with $M = 6$ (b) ML

Figure 9: Classification images using C_2

ACKNOWLEDGMENTS

The SAR data used in this study were provided by National Space Development Agency of Japan (NASDA). The authors would like to thank JPL, NASA, Dr Shimada at NASDA and Dr Hanaizumi at Hosei University, Japan for the interferometric SAR software. The image processing facilities are supported by the University of London Inter-Collegiate Research Services.

REFERENCES

Fujisawa, S., Rosen, P. A., 1998. Crustal deformation measurements using repeat-pass JERS 1 synthetic aperture radar interferometry near the Izu Peninsula, Japan, Journal of Geophysical Research, 103(B2), pp. 2411–2426.

Ito, Y., Omatu, S., 1997. Category classification method using a self-organizing neural network, International Journal of Remote Sensing, 18(4), pp. 829–845.

Kohonen, T., 1997. Self-Organizing Maps. Springer, Berlin, pp. 203–217.

Lee, H., Liu, J. G., 1999. Spatial decorrelation due to topography in the interferometric SAR coherence imagery. In: IEEE International Geoscience and Remote Sensing Symposium (IGARSS'99) Proceedings, Hamburg, Germany, Vol. 1, pp. 485–487.

Richards, J. A., 1993. Remote Sensing Digital Image Analysis. Springer-Verlag, Berlin, pp. 271–275.

Yonezawa, C., Takeuchi, S., 1999. Detection of urban damage using interferometric SAR decorrelation. In: IEEE International Geoscience and Remote Sensing Symposium (IGARSS'99) Proceedings, Hamburg, Germany, Vol. 2, pp. 925–927.

Zebker, H. A., Villasenor, J., 1992. Decorrelation in interferometric radar echoes. IEEE Transactions on Geoscience and Remote Sensing, 30(5), pp. 950–959.